Spread-Spectrum Modulated Multi-Channel Biosignal Acquisition Using a Shared Analog CMOS Front-End

This article has been accepted for publication in IEEE Transactions on Biomedical Circuits and Systems. This is the author's version which has not been fully edited and content may change prior to final publication. Citation information: DOI 10.1109/TBCAS.2023.3317188

Spread-spectrum modulated multi-channel biosignal acquisition using a shared analog CMOS front-end

Samprajani Rout, *Student Member, IEEE,* Bert Monna, Fabio Pareschi, *Member, IEEE,* Gianluca Setti, *Fellow, IEEE,* and Wouter Serdijn, *Fellow, IEEE*

***Abstract*—The key challenges in designing a multi-channel biosignal acquisition system for an ambulatory or invasive medical application with a high channel count are reducing the power consumption, area consumption and the outgoing wire count. This paper proposes a spread-spectrum modulated biosignal acquisition system using a shared amplifier and an ADC. We propose a design method to optimize a recording system for a given application based on the required SNR performance, number of inputs, and area. The proposed method is tested and validated on real pre-recorded atrial electrograms and achieves an average percentage root-mean-square difference (PRD) performance of 2.65% and 3.02% for sinus rhythm (SR) and atrial fibrillation (AF), respectively by using pseudo-random binary-sequence (PRBS) codes with a code-length of 511, for 16 inputs. We implement a 4-input spread-spectrum analog front-end in a $0.18\,\mu$m CMOS process to demonstrate the proposed approach. The analog front-end consists of a shared amplifier, a 2^{nd} order $\Sigma\Delta$ ADC sampled at $7.8\,$MHz, used for digitization, and an on-chip 7-bit PRBS generator. It achieves a number-of-inputs to outgoing-wire ratio of 4:1 while consuming $23\,\mu$A/input including biasing from a $1.8\,$V power supply and $0.067\,\text{mm}^2$ in area.**

***Index Terms*—spread-spectrum modulation, multi-channel signal acquisition, linear-feedback shift register, Gold codes, ECG, atrial electrograms, sigma-delta converter, biosignal acquisition**

I. Introduction

ATRIAL electrograms (AEGs) are biosignals recorded on the surface of the atria, whereas electrocardiograms (ECGs) are recorded on the surface of the body, both of which help doctors and medical researchers understand the propagation of electrical signals in the heart and diagnose cardiac abnormalities such as atrial fibrillation (AF). ECGs are vector summations of the epicardial signals acquired non-invasively on the body surface, whereas AEGs offer high spatio-temporal information acquired invasively on the epicardial or the endocardial surface [1]. AEGs are obtained invasively or minimally invasively during open-heart surgery or a catheter operation, respectively. For minimally invasive surgeries, typically, a $6\,$Fr ($2\,$mm) catheter tube is used, which poses a strict constraint on the area and the maximum number of outgoing wires. Current techniques for acquiring AEGs require a long cable connecting a multi-electrode flexible array [1] placed on the epicardial surface and the acquisition module for high-density mapping. The limitations of the current solution can be listed as follows: a) interference due to the long cable degrading signal quality; b) limited maneuverability as the number of outgoing wires from the array is equal to the number of electrode inputs, and c) area constraints for minimally-invasive applications.

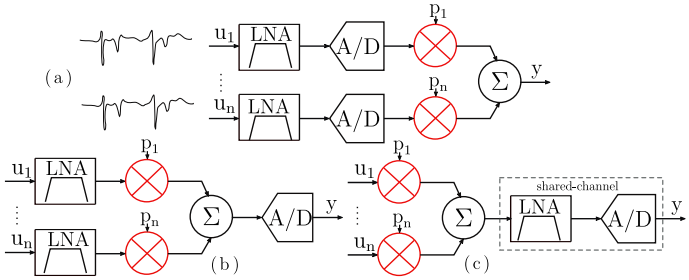

Fig. 1: Approaches to implementing spread-spectrum modulation: (a) in the digital domain (conventional), (b) in the analog domain, after amplification (conventional), and (c) in the analog domain, before amplification (proposed).

In a traditional N-input system, the total number of amplifiers, ADCs, and outgoing wires equals the number of inputs N, thus scaling area, power, and outgoing wire count linearly by N. To address these limitations, one can use channel-sharing techniques such as time-division (TDM), frequency-division (FDM), or code-division multiplexing (CDM). TDM requires a dedicated amplifier per input [2] and does not utilize the total bandwidth of the ADC effectively. The order of the inputs is also important for signal reconstruction in the digital domain. [3] uses TDM to acquire signals after the electrode but requires a high-bandwidth front-end to meet settling and noise requirements. FDM based on frequency modulation (FM) uses separate frequency bands simultaneously [4] and requires a dedicated oscillator, a bandpass amplifier, and an off-chip high-Q inductor per input posing a constraint on the area and power. FDM based on amplitude modulation (AM) would require a very high dynamic range (>100 dB) [5] ADC due to voltage summation of N inputs. [6] implements CDM using a dedicated amplifier and filter circuitry before code modulation, whereas [7] modulates the signals at the input using orthogonal codes. CDM offers (a) increased capacity, allowing multiple users to share the same band, (b) improved signal quality as it suppresses interference and band-limited noise, (c) improved security, a unique code encodes each input, and (d) simpler

S. Rout and W. A. Serdijn are with the Section Bioelectronics, Department of Microelectronics, Delft University of Technology, 2628 Delft, The Netherlands (e-mail: s.rout@tudelft.nl; w.a.serdijn@tudelft.nl). W.A. Serdijn is also with the Department of Neuroscience, Erasmus Medical Center, the Netherlands.

B. Monna is with Phosphoenix, 2623 Delft, The Netherlands (e-mail: bert@phosphoenix.nl).

F. Pareschi is with the Department of Electronics and Telecommunications of the Politecnico di Torino, Italy (e-mail: fabio.pareschi@polito.it).

G. Setti is with CEMSE, King Abdullah University of Science and Technology (KAUST), Saudi Arabia (e-mail: gianluca.setti@kaust.edu.sa).

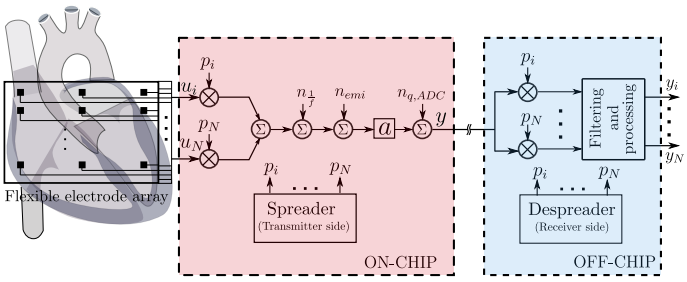

Fig. 2: Linear model of the proposed spread-spectrum front-end for atrial electrogram acquisition.

implementation, as compared to FDM. Therefore, CDM, as illustrated in Fig 1, is chosen as the channel-sharing technique in this work. Fig. 1 shows the block diagram of conventional spread-spectrum digital (Fig. 1a) and analog (Fig. 1b) front-end (FE), which requires dedicated FE resources per input. Fig. 1c shows the proposed spread-spectrum FE. Modulating the signal early in the signal chain can minimize the effects of unwanted band-limited signals with finite power such as electro-magnetic-interference or $\frac{1}{f}$ noise, and offset of the following CMOS blocks. Fig. 2 shows a linear model of the proposed spread-spectrum FE for acquiring atrial electrograms. The proposed approach a) enables high-density signal-wavefront mapping from a 2D electrode array while reducing the outgoing wire count, (b) reducing area by sharing FE channel resources, and (c) reducing flicker noise and offset of the FE CMOS block. The acquired signal is written as,

$$y(t) = \{\sum_{i=1}^{N} u_i(t)p_i(t) + n_f(t) + n_{th}(t) + n_{emi}(t)\}A + n_{q,adc}(t) \tag{1}$$

where $y(t)$ is the total signal acquired, $u_i(t)$ is the signal from the i_{th} electrode and $p_i(t)$ is the code-sequence uniquely assigned to the i_{th} signal, $n_f(t)$ is band-limited $\frac{1}{f}$ noise, $n_{th}(t)$ is wide-band thermal noise, $n_{emi}(t)$ is interference due to EMI, $n_{q,adc}(t)$ is the quantization noise of the ADC, and N is the number of inputs. The received signal is correlated with the replica of the code sequence on the receiver side. The reconstructed signal, $y_i(t)$, can be written as,

$$y_i(t) = y(t)p_i(t) \tag{2}$$

$$= p_i(t)A\sum_{i=1}^{N} u_i p_i(t) + p_i(t)\{A(n_f(t) + n_{emi}(t)) + n_{q,adc}(t)\} \tag{3}$$

$$= Au_i(t) + p_i\{A(n_f(t) + n_{emi}(t)) + n_q(t)\} \tag{4}$$

Given that the the signal energy of p_i is distributed over a large frequency band, from Eq. 4, the u_i^{th} signal is recovered while $\frac{1}{f}$ noise, electromagnetic interference and offset are modulated by the p_i^{th} sequence and are filtered out using a low-pass filter.

The rest of the paper is organized as follows. In Section II, a classification of exisiting modulation schemes is proposed. In Section III, a method to optimize a spread-spectrum FE for acquiring biosignals by selecting code-length, modulation frequency, and the number of inputs is discussed. This approach has been validated using real pre-recorded biosignals using two types of commonly used codes, Walsh-Hadamard (WH) and pseudo-random codes. Section IV describes the system architecture and circuit implementation of the spread-spectrum modulated FE. Measurement results of a 4-channel spread-spectrum amplifier with a $\Sigma\Delta$ modulator implemented in $0.18\,\mu$m CMOS technology are presented in Section V. Finally, conclusions are drawn in Section VI.

II. Proposed Classification

In this section, we propose a classification of modulation techniques based on the properties (or degrees of freedom) of the modulating signal (also known as the carrier wave), as shown in Figure 3. The degrees of freedom are (a) periodicity, (b) discretization in time, and (c) discretization in amplitude of the carrier wave, as shown along the x-, y-, and z-axis, respectively. To the authors' best knowledge, such a classification does not yet exist in the literature. Such a classification can give rise to newer modulation approaches that may or may not have been explored yet. Subsections II-A through II-C describe the degrees of freedom. Subsection II-D elaborates on the exisiting modulation approaches.

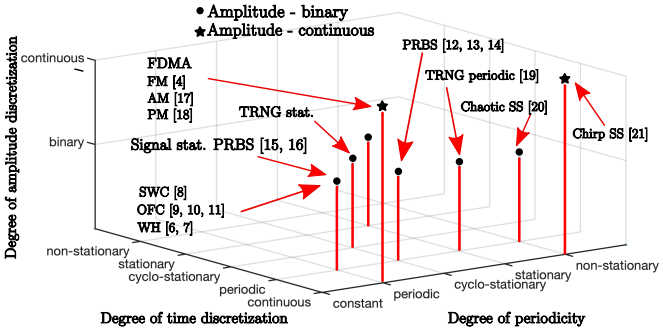

Fig. 3: Proposed classification of modulation techniques

A. Degree of periodicity

The degree of periodicity of modulating signals refers to the occurence of symbols 0's and 1's and can be categorized into constant, periodic, stochastic-stationary, stochastic-cyclostationary and stochastic non-stationary, respectively.

- Constant: The symbols of the modulating waveform do not change (i.e., remain constant).
- Periodic: The signal is completely specified with respect to time and repeats with a period T_o.
- Stochastic-stationary: The signal is not fully specified with respect to time. However, the statistics are time-invariant. The mean is constant. The autocorrelation $R_X(t_1, t_2)$ only depends on time lag τ and is not a function of time t.
- Stochastic-cyclostationary: The statistics of the signal may vary periodically with time. The mean is cyclic in time t with a period T_o. Autocorrelation is a function of time period T_o.

TABLE I: Some example modulation techniques and applications

Paper	Technique	Application
[8]	Square-wave chopping (SWC)	Performance enhancement
[9], [10], [11]	Orthogonal freq. chop. (OFC)	Multi-channel recording
[6], [7]	Walsh Hadamard (WH)	Multi-channel recording
[12], [13], [14]	Pseudo-random binary seq. (PRBS)	Performance enhancement
[15]	Pseudo-random binary seq.(PRBS)	Compressed sensing
[16]	Signal stat. PRBS modulation	Single-channel recording
[4]	Frequency modulation (FM)	Single-channel recording
[17]	Amplitude modulation (AM)	Communication systems
[18]	Phase modulation (PM)	Communication systems
[19]	True random number gen. (TRNG)	Hardware security
[20]	Chaotic modulation	Communication systems
[21]	Chirp modulation	Communication systems
This work	PRBS modulation	Multi-channel recording

- Stochastic non-stationary: The statistics change over time, i.e., the mean changes with time. Autocorrelation is a function of time t.

B. Degree of time discretization

Time discretization refers to the sampling instant in time and can be categorized as:

- Continuous: Time is continuous.
- Periodic: The sampling frequency is fixed.
- Stochastic-stationary: The sampling frequency is randomly varying, but is stationary.
- Stochastic-cyclostationary: The sampling frequency is randomly varying and the statistics vary periodically with time with a time period T_o. If the sampling instant of the signal is determined by other parameters such as thresholding of the input signal, then the clock incorporates the properties of the inputs signal. In case of adaptive sampling, the rate of the clock depends on the activity of the input signal.
- Stochastic-non-stationary: The sampling frequency is randomly varying and its statistics change with time.

C. Degree of amplitude discretization

Amplitude discretization can be categorized as:

- Discrete-M-ary values: The signal can assume a value from a well-defined set of outcomes. In general, a set of 2 (e.g., {0,1} or {-1,1} are binary sets), a set of 3 (e.g., {-1, 0, 1} is a ternary set) or a limited set of values (e.g., M-ary set) can be used. The total probability of all outcomes is the summation of individual probabilities and equals 1.
- Continuous values: The signal can assume any real value.

D. Existing modulation techniques

Input signals can be modulated with a waveform resulting from the orthogonal combination of the above-mentioned degrees of freedom. In this sub-section, a few existing modulation techniques are classified and placed on the three axes of a 3D grid to accomodate the three degrees of freedom, as shown in Fig. 3. Table I summarizes the modulation type and its corresponding application. [8] uses square-wave modulation (chopping, auto-zeroing, or correlated double-sampling) for improving the circuit's performance, i.e., reducing offset and flicker noise. Spread-spectrum clocking can be used with a chopper-stabilized amplifier which reduces inter-modulation distortion [12], [13]. PRBS modulation is used together with a $\Sigma\Delta$ modulator to reduce substrate noise [14]. [9]–[11] are examples of an orthogonal modulation technique, also referred to as 'multi-frequency chopping'. All these techniques lie at $\{periodic, periodic, binary\}$ in Fig. 3. The modulating wave is characterized by orthogonal periodic sequences which assume binary amplitude values, i.e., ± 1. Conventional code-division multiplexing (CDM) lies at $periodic$ (orthogonal) or $cyclostationary$ on the x-axis, $periodic$ on the y-axis and $binary$ on the z-axis. [7] and [6] use orthogonal Walsh-Hadamard codes to acquire signals from multiple channels. [4], [17] and [18] are examples of conventional frequency division multiplexing (FDM) which lie at $\{periodic, continuous, continuous\}$. [16] acquires signals from a single input using pseudo-random binary sequences (PRBS) while the sampling frequency varies in a stochastic-cyclostationary fashion based on the input signal. Here, the carrier signal is statistically correlated to the input. Another example of a correlated chipping sequence with respect to the input-signal statistics is rakeness-based compressed sensing [15]. The carrier waveform can be either correlated or uncorrelated with the input signal. In standard compressed sensing, the input matrix is uncorrelated with the input signal characteristics [22].

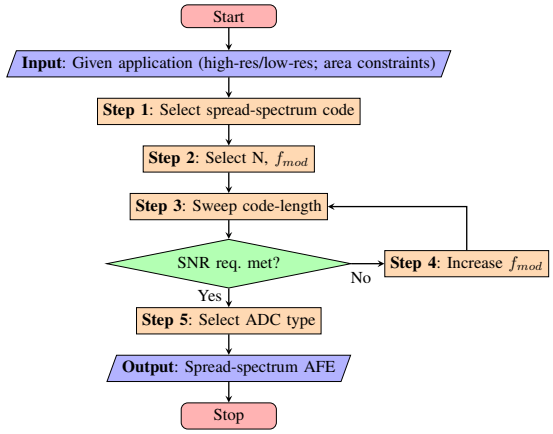

Fig. 4: Design strategy for multi-channel spread-spectrum analog front-ends.

III. Proposed Design Methodology

In this section, we propose a design method based on spread-spectrum modulation for multi-channel bio-signal acquisition. For a given number of channels, power consumption, area, and the application-derived performance requirements, the proposed design method can be carried out as illustrated in Figure 4. Starting with the target application as the input, the design strategy follows from 5 steps, as described in sub-sections III-A to III-D, arriving at an optimal spread-spectrum AFE at the output. Finally, sub-section III-F illustrates the proposed design method on real pre-recorded AEGs.

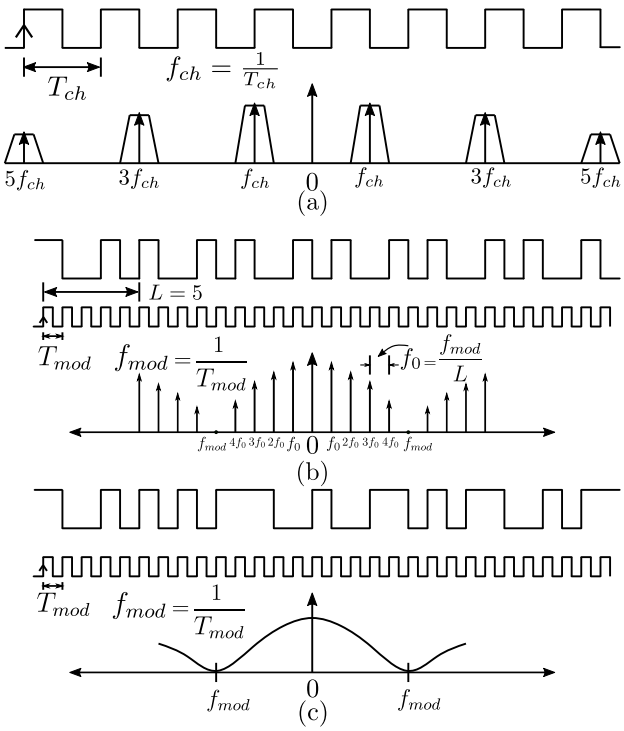

Fig. 5: Time-domain and frequency-domain representation of modulation signals: a) Periodic; b) Cyclostationary random; c) Stationary random. f_{ch} and f_{mod} refer to the modulation frequency of periodic and (pseudo-) random signals, respectively.

A. *Input*: Application requirement

Based on the target application, one or more design parameters, such as power consumption, area, and resolution are more critical than the others. We consider two application cases of the acquisition of multi-channel AEGs here:

- Multi-channel PRBS codes for low-resolution recording.
- Multi-channel WH codes for high-resolution recording.

Multi-channel PRBS codes can, e.g., be used when we wish to track the propagation of the cardiac wavefront and generate an activation map [1], which requires only low-resolution and low-bandwidth signals. Multi-channel WH orthogonal codes can be used when we wish to acquire high-resolution signals for identification of detailed features of the AEG [23].

B. *Step 1*: Selection of codes

Based on the degree of periodicity from the proposed classification, modulation codes can be periodic, cyclostationary random or stationary random. Fig. 5 shows the time-domain and frequency-domain representations of periodic, cyclostationary, and stationary random codes, and which are elaborated in the following paragraphs.

Periodic codes: An example of a periodic modulating signal (or square-wave signal) is conventional chopping, as shown in Fig. 5a where f_{ch} is the chopping signal. Consider a periodic train of pulses characterized by amplitude $\pm$A and a duration of τ. Let $v(t)$ be a periodic signal with period $T_{ch} = \frac{1}{f_{ch}}$ defined by,

$$v(t \pm mT_{ch}) = v(t), \quad -\infty < t < \infty \tag{5}$$

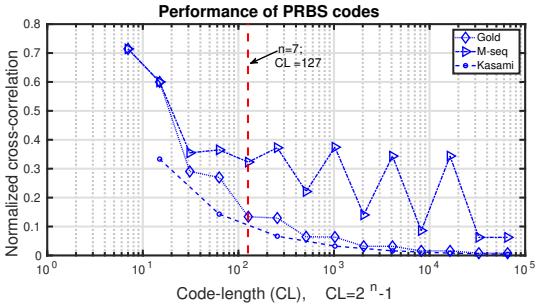

Fig. 6: Theoretical limit of cross-correlation of PRBS codes. Note: Y-axis plots normalized cross-correlation (= ratio of peak cross-correlation to peak auto-correlation).

where m is an integer. The spectrum of a signal is computed using the Fourier integral. Since the integrability condition is not met, the Fourier integral cannot be directly computed [24]). To calculate the Fourier integral, the signal is truncated, and the range of integration over $\frac{-T_{ch}}{2} \leqslant t \leqslant \frac{T_{ch}}{2}$ is taken, where

$$v(t) = \left\{ \begin{array}{ll} A, & \text{for } |t| \leq \tau/2 \\ 0, & \text{for } |t| \geq \tau/2 \end{array} \right\}$$

The Fourier expansion is given by $v(t) = \sum_{n=-\infty}^{\infty} c_n e^{j2\pi n f_{ch} t}$, for $n = 0, 1, 2$ where $c_n = \frac{A\tau}{T_{ch}} sinc\{nf_{ch}\tau\}$. Note that, for periodic signals, the amplitude spectrum consists of a line spectrum where the lines have uniform spacing f_{ch}. By the Wiener-Khinchine theorem, the power of the signal is given by $P_v(f) = \sum_{n=-\infty}^{\infty} |c_n^2| \delta(f - nf_{ch})$.

Orthogonal codes such as WH codes also lie at *periodic* on the degree of periodicity axis, as shown in Fig. 3. The WH transform is a non-sinusoidal orthogonal transformation technique that decomposes an arbitrary vector of dimension 2^m into a set of basis functions called Walsh functions which are square or rectangular waves with values +1 or -1. It performs an orthogonal symmetric and linear operation on the input vector.

Spread-spectrum codes: Random codes can be used to spread the energy of the input signal to a larger bandwidth. For a random signal, the spreading bandwidth is infinite since an infinitely long sequence leads to a continuous spectrum. The PSD of a random signal $v(t) = \sum_{n=-\infty}^{\infty} a_n f(t - nT_{mod})$, where T_{mod} is the duration of 1 bit, is given by $P_v(f) = T_{mod}(sinc\pi f T_{mod})^2$ [25] as also shown in Fig. 5c. However, in practice, random code sequences are generated using pseudo-random generators since a replica of the code sequence is needed to recover the input signal. Pseudo-random binary sequences (PRBS) are cyclostationary, as shown in Figure 5c. A popular choice for implementing PRBS codes is employing linear feedback shift registers (LFSRs). In the design of an LFSR, the code sequences are replicated by choosing the same initial state and coefficients. Let $p(t)$ be a cyclostationary sequence that assumes an amplitude of ± 1 randomly at a rate of f_{mod} and the sequence repeats after code length L, given by the time-period $T_0 = LT_{mod}$, where $T_{mod} = \frac{1}{f_{mod}}$, $L = 2^n - 1$, and n is the number of bits of the LFSR. $p(t) = \sum_k a_k q(t - kT_0), k \in Z, a_k \in [1, -1]$ is a cyclosta-

tionary sequence and $q(t) = \sum_{n=0}^{L-1} c_n s(t - nT_{mod}), c_n \in Z$ is a stationary random sequence whose length is given by L. Since the function $p(t)$ is periodic with T_0, by the Wiener Khinchine theorem, the PSD is a line spectrum given by,

$$S_p(f) = \left[\sum_{m=-\infty}^{\infty} \delta(f - mf_o)\right] \frac{L+1}{L^2} \left(\frac{sin\pi f/f_c}{\pi f/f_c}\right)^2 + \frac{1}{L^2}\delta(f) \quad (6)$$

where $f_0 = \frac{1}{T_{mod}}$. An example with $L = 5$ is shown in Figure 5b.

Some examples of PRBS codes are maximum-length (ML) sequences, Gold codes, and Kasami codes, and they are used in communication systems to encode multiple signals. These codes are non-orthogonal and have varying cross-correlation properties as shown in Fig. 6. The most important selection criterion in acquiring multiple biosignals is suppressing interference from other signals in the shared channel. The code length, L, is given by $L = 2^n - 1$, where n is an integer corresponding to the polynomial order used to generate the code. n is *odd* for ML, Gold, and *even* for Kasami codes. The peak auto-correlation is given by L. The peak cross-correlation values for Gold codes is given by $t(n)$, where $t(n) = 2^{(n+1)/2}$, m is odd; $2^{(n+2)/2}$, in case n is even; for Kasami codes, $t(n)$ is given by $2^{n/2} + 1$ [26]–[28]. Fig. 6 shows that the cross-correlation performance improves with increasing n bit (or L) for ML, Gold, and Kasami codes. Secondly, we can observe that for a given L, Kasami codes are optimal as they approach the Welch lower bound on peak cross-correlation [29]. However, the performance gap between Kasami and Gold codes reduces at higher values of L. Kasami codes offer marginal performance enhancement over Gold codes at the cost of higher implementation complexity. Thirdly, odd-order ML and Gold sequences offer lower cross-correlation performance than even order.

C. ***Step 2,3***: *Selection of N and f_{mod}; Sweep code-length*

In this sub-section, the number of inputs, N, the code length (L), and the selection of the modulation frequency, f_{mod}, are discussed. If the interfering signals are unknown but have finite power, the input signal may overlap with the interferer. If the interferers are known (e.g., flicker noise), the input signal can be spread to a non-overlapping frequency band. In Figure 7, it can be seen that spread-spectrum modulation suppresses $\frac{1}{f}$ noise. As an example, in Figure 7a, a 3-bit PRBS code (L=7) with a modulation frequency f_{mod}=12.8 kHz is used to modulate and demodulate an input signal, f_{in}=0.108 kHz with a bandwidth f_b=0.4kHz. It can be observed that the $\frac{1}{f}$ noise reduces and the lowest tone f_0 is at $\frac{f_{mod}}{7}$=1.8kHz. Figure 7b shows the effect of L for varying values of the spreading gain G, given by: $G = \frac{f_{mod}}{f_b}$ on the SNR performance. At lower values of G, there is a marginal improvement of SNR even when the number of LFSR bits increases. For a given G, there is an optimal value of L at which the SNR is maximal. The peak shifts with increasing G. After the peak, the curve shows a decrease in SNR. This decrease is because the smallest tone given by f_0 is within the signal bandwidth, and some of the $\frac{1}{f}$ noise is in-band. A larger L implies a larger spreaded

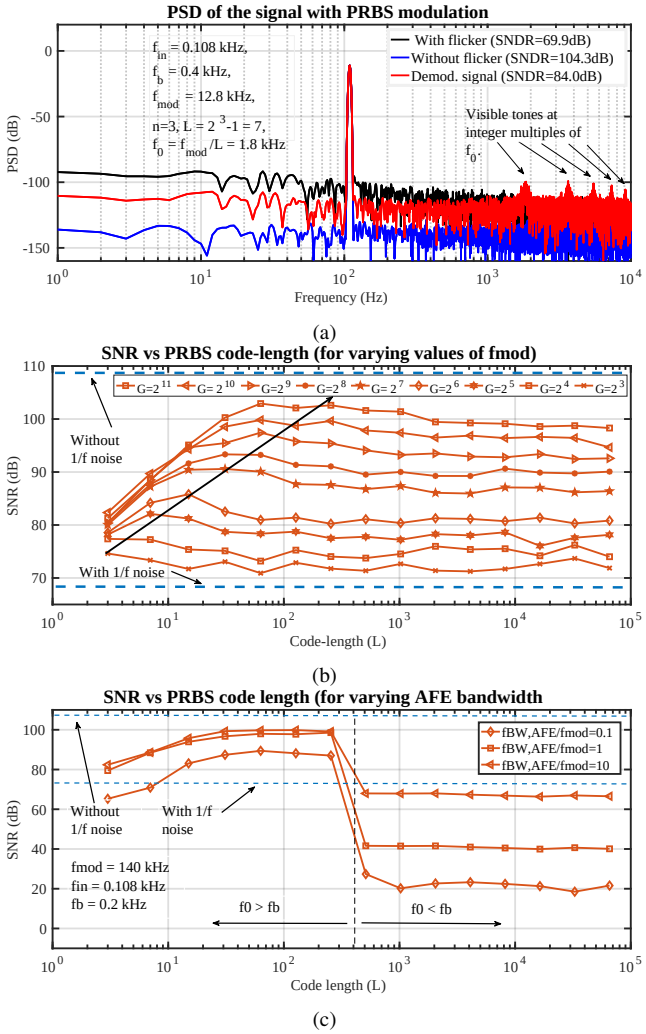

Fig. 7: Single channel PRBS modulation. (a) PSD of a single channel modulated and demodulated with a 3-bit PRBS code. (b) Effect of spreading gain (G = $\frac{f_{mod}}{f_b}$). As G increases, f_0 (= $\frac{f_{mod}}{L}$) moves higher. (c) Effect of AFE bandwidth.

bandwidth. However, f_{mod} should be high enough to push f_0 outside f_b. The two blue dashed lines show the minimum and maximum achievable SNR levels corresponding to, with, and without $\frac{1}{f}$ noise, respectively.

Impact of limited AFE bandwidth: The AFE is responsible for amplifying the entire spectrum, and it requires a minimum bandwidth equal to the modulation frequency, denoted as f_{mod}. If the amplifier's bandwidth is lower than f_{mod}, some of the signal will be lost and cannot be recovered. When using shorter code-lengths, a significant amount of information is lost at a given f_{mod}. On the other hand, increasing the code-length spreads the signal over a wider bandwidth, resulting in improved performance. However, when the code-length is large and f_0 falls within the signal bandwidth, the SNR performance drops which is clearly demonstrated in Figure 7c.

Multi-channel acquisition: For acquiring multiple inputs using a shared channel, the maximum number of inputs for a given n-bit LFSR is given by Euler's totient equation, $C = \frac{1}{N}\Pi\{P_i^{\alpha_i - 1} \cdot (P_i - 1)\}$, where P_i are the prime factors of

TABLE II: Performance of PRBS codes on multi-channel acquisition

n	$L(=2^n\text{-}1)$	No. of codes	Avg. SNR (in dB)				
			N=2	**N=4**	**N=8**	**N=16**	**N=32**
3	7	2	16.90	-	-	-	-
4	15	2	23.52	-	-	-	-
5	31	6	29.82	27.16	-	-	-
6	63	6	35.98	33.32	-	-	-
7	127	18	42.07	39.40	38.14	36.27	-
8	255	16	48.13	45.46	44.18	42.31	-
9	511	48	54.16	51.49	50.21	48.35	43.91
10	1023	60	45.10	30.63	29.56	22.19	20.61
11	2047	176	31.73	29.23	24.95	21.87	17.87
12	4095	144	32.94	28.36	23.68	20.16	17.01
13	8191	630	30.94	26.42	23.17	19.53	16.67
14	16383	756	30.77	26.95	22.87	19.97	16.69
15	32767	1800	28.32	27.04	24.38	20.23	16.88
16	65535	2048	31.04	26.26	22.56	19.35	16.55

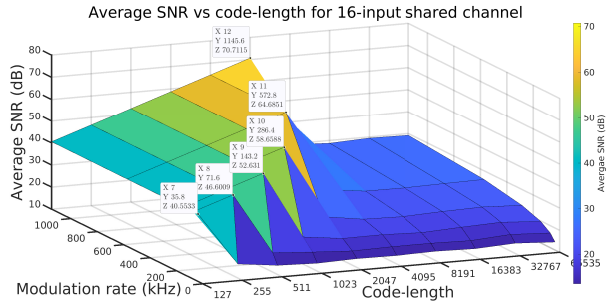

Fig. 8: Multi-channel acquisition for 16-input shared channel with varying modulation frequency.

L and α_i is the power of the ith factor [30]. In Table II, the acquisition performance is shown for N = 2, 4, 8, 16 and 32 for f_b=100 Hz and f_{mod}=153.6 kHz. A smaller signal bandwidth allows for either (a) a smaller modulation frequency (f_{mod}) and thus a smaller amplifier bandwidth ($f_{BW,AFE}$) for the same code length (L) and number of channels (N), or (b) a larger L, and thus a larger signal-to-noise ratio (SNR), for the same f_{mod}, N and $f_{BW,AFE}$, or (c) a large N and a larger L for the same f_{mod}, SNR and $f_{BW,AFE}$. As given in the table, using a code-length of 127 (which can be generated by a 7-stage PRBS generator), the maximum SNR that can be achieved is 39 dB for a 2-input shared channel, given that the smallest tone (f_0) lies outside the signal bandwidth. For a shared channel, the maximum average SNR decreases with an increasing number of inputs. On the highlighted row in Table II, for a 4-input channel, the maximum achievable SNR is 39.4 dB. If a higher average SNR is desired, it can be achieved by increasing f_{mod} and selecting a longer L.

D. *Step 4, 5 Increase* f_{mod}

The modulation frequency can be increased linearly to achieve higher performance at a corresponding code length. In Fig. 8, it is shown that for a 16-input shared channel, an average SNR of 64 dB can be achieved by using a code-length of 2047 at a modulation rate of 572.8 kHz for a total signal bandwidth of 1.6 kHz (16 x 100 Hz). Also, it can be seen that using a 7-bit LFSR @f_{mod}=40.5 kHz, for 16 channels, the maximum SNR that can be achieved is 35.8 dB.

E. *Comparison with other modulation techniques*

In this sub-section, the requirements of PRBS modulation, WH modulation and orthogonal frequency chopping are qualitatively compared in terms of bandwidth and area. Consider a signal bandwidth f_b, number of inputs N and a code length = 128. For PRBS modulation, the minumum required modulation frequency is given by $f_{mod} = 2 \times 127 \times f_b$, with a maximum capacity of N = 18, whereas, for WH modulation, it is given by $f_{mod} = 2 \times 128 \times f_b$ with a maximum capacity of N = 128. For orthogonal frequency chopping, the minimum required frequency is $f_{mod} = 2 \times 2^7 \times f_b$, with a maximum capacity of N = 7. So, for a given total bandwidth, WH modulation is most efficient, followed by PRBS codes and orthogonal frequency chopping. From a hardware viewpoint, PRBS codes are easy to generate since they require a few digital gates and consume negligible power and area [31]. The number of D flip-flops in a PRBS generator for a given L scales with $log_2(L)$. Implementing orthogonal codes requires look-up tables whose length scales with the power of 2, as the number of inputs increase. In practice, orthogonal codes have non-zero cross-correlation as shown in [7]. In this work, we select Gold codes since they consume the least area for the required performance.

F. *Illustration of the design method: Validation on real pre-recorded AEG signals*

The proposed technique is tested and validated without any pre-processing on real pre-recorded atrial electrograms from the Erasmus Medical Centre, Rotterdam. Hospital recordings tend to be less clean (due to noise and interference) than synthetically modeled datasets or clean datasets available in public databases (e.g., MIT-BIH). The amplitude of AEGs varies from 1-10 mVpp depending on the size and the recording location in the heart. The signal bandwidth typically extends from 0.5 Hz to 200 Hz. The flexible electrode array contains 192 electrodes, each of which has a diameter of 0.45 mm and an inter-electrode distance of 2 mm [1]. Increasing the electrode diameter may lead to loss of spatial information, while decreasing it will increase the electrode impedance. 16 sinus rhythm (SR) and atrial fibrillation (AF) AEG signals as shown in Figs. 9a - 9b are encoded using spread-spectrum codes, summed, and demodulated. Figures 9c - 9f show the performance of PRBS modulation using L=127 and 511, at f_{mod}=35 kHz and 140 kHz, respectively for SR (input 2) and AF AEG (input 2). AF exhibits a larger residual error than SR AEG, as seen in Figs. 9g-9h, due to significantly higher signal activity. SR exhibits a worse performance in certain parts of the segment than AF due to sharp peaks and loss of those peaks in the reconstructed signal. SR yields better average recovery at higher parameter settings than AF, as shown in Table III. The effectiveness of PRBS and Walsh-Hadamard codes with different parameter configurations can be compared using the percentage root-mean-square difference (PRD), which quantifies the similarity between the original and reconstructed signal. A lower PRD value indicates better performance. The average PRD values are obtained by calculating over AEGs lasting 2 s and averaged over 16 inputs. For a bandwidth of

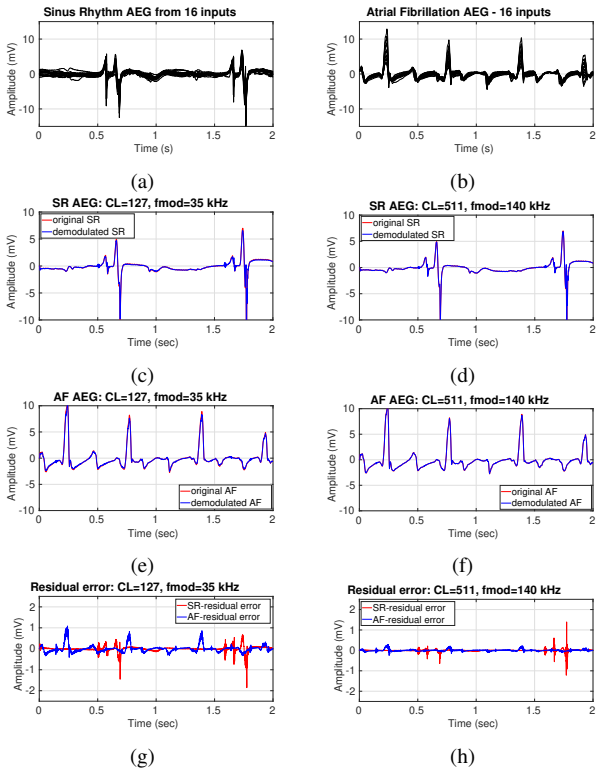

Fig. 9: Validation of PRBS modulation on pre-recorded (a) SR and (b) AF AEGs from 16 inputs. Demodulated (c) SR and (b) AF AEG with L=127, f_{mod}=35 kHz. Demodulated (e) SR and (f) AF AEG with L=511, f_{mod}=140 kHz. Residual error given by the difference between original and demodulated signals for (g) L=127, f_{mod}=35 kHz and (h) L=511, f_{mod}=140 kHz.

TABLE III: Average PRD performance

Parameter setting				Average PRD (%)	
Type of code	No. of inputs	Code-length	Modulation freq.	SR AEG	AF AEG
PRBS	16	127	20 kHz	42.9	50.7
PRBS	16	127	35 kHz	14.9	13.78
PRBS	16	127	70 kHz	10.8	13.1
PRBS	16	127	140 kHz	10.7	13.1
PRBS	16	511	80 kHz	23.1	27.45
PRBS	16	511	140 kHz	6.2	3.6
PRBS	16	511	280 kHz	2.65	3.02
PRBS	16	511	560 kHz	2.5	3.01
Walsh	16	16	4 kHz	36.3	23.6
Walsh	16	16	8 kHz	6.9	1.2
Walsh	16	16	16 kHz	0.25	0.39
Walsh	16	16	32 kHz	0.1	0.2
PRBS	4	127	20 kHz	30.6	32.5
PRBS	4	127	35 kHz	4.7	3.1
PRBS	4	127	70 kHz	2.3	2.47
PRBS	4	127	140 kHz	2.3	2.4

f_b = 200 Hz and L = 127, the optimum modulation frequency is 70 kHz with mean PRD values of 10.8 and 13.1 for SR and AF, respectively. The PRD performance for SR and AF improves to 2.65 and 3.02, respectively, when L = 511 and f_{mod} = 280 kHz. In this illustration, the optimal parameters for a given code length for PRBS and Walsh codes are shown in the highlighted row of Table III. A marginal improvement in PRD performance is observed beyond the optimum f_{mod} for both PRBS and WH codes. The proposed technique was evaluated using PRBS codes on 4 inputs with a code length of 127. At f_{mod} = 35 kHz, the PRD performance for SR and AF improved to 4.7% and 3.1% respectively, compared to higher values of 14.9% and 13.78% when 16 inputs were employed.

IV. System Architecture and Circuit Implementation

To validate the proposed design strategy for spread-spectrum acquisition of AEGs, a 4-input shared amplifier and a $\Sigma\Delta$ ADC are implemented in a standard 0.18 μm CMOS IC process. AEGs are unipolar recordings and the reference is shared across all the inputs. The reference electrode is large and its impedance does not add considerably to the total impedance seen by each channel. Mismatch between electrodes leads to negligible common-mode to differential-mode conversion as the input impedance of the front-end is much larger than the mismatch in electrode impedance. Each input utilizes a large off-chip decoupling capacitor to block any resulting DC offset due to the gold metal and cardiac tissue interaction. Figure 10 shows the block diagram of the proposed system architecture. Subsections IV-A - IV-C elaborate on the various blocks.

A. Analog front-end

Each channel consists of a modulator, a shared amplifier and a shared ADC. The signals are multiplied by spread-spectrum codes given by p_i. Input capacitances (C_{in}) convert the input voltage signals into currents. The summation of these currents takes place at the virtual ground node of the opamp. Four gain settings (G=4/8/16/32) are available for different input amplitude ranges (10/5/2.5/1.25 mVpp) corresponding to AEGs recorded on the epicardium. The gain settings are implemented by the ratio of capacitances C_{in} and C_{fb}. C_{in} is implemented as a variable capacitor bank (400fF, 800fF, 1.6pF, 3.2pF) with CMOS transmission gate (TG) switches controlled digitally. The modulator is implemented by four switches which are driven by a non-overlapping clock generator. The switch is implemented by a CMOS TG which offers a higher linearity and range for large amplitude signals as compared to NMOS or PMOS switches. The effective ON resistance of the switch of a TG is lower than that of a NMOS or a PMOS switch. The switches are sized optimally for lower ON resistance and lower charge injection. Off-chip capacitors are used with the flexible-electrode array to ensure patient safety. Since the electrodes are used directly on the surface of the heart and do not use gel, the expected DC offset level at the tissue-electrode interface is low. Therefore, this architecture does not employ a dedicated high-pass loop per channel to reject offset which would otherwise saturate the amplifier [32].

The opamp is implemented by a two-stage Miller-compensated topology as shown in Fig 11a. A two-stage opamp with continuous-time common-mode feedback (CMFB) is chosen to achieve high DC gain, high linearity and to drive the input resistance of the ADC. The second stage is designed to meet high signal-swing requirements for four inputs. To achieve lower $\frac{1}{f}$ noise, the first stage has a PMOS differential input pair biased in weak-inversion saturation. The simulated DC gain of the two-stage opamp is 100 dB. The AC bandwidth extends from sub-Hz to 150 kHz. Pseudo-resistors R_{ps} are implemented using PMOS transistors biased in weak-inversion triode and provide a DC path from the output to the input, thereby setting the input common-mode voltage equal

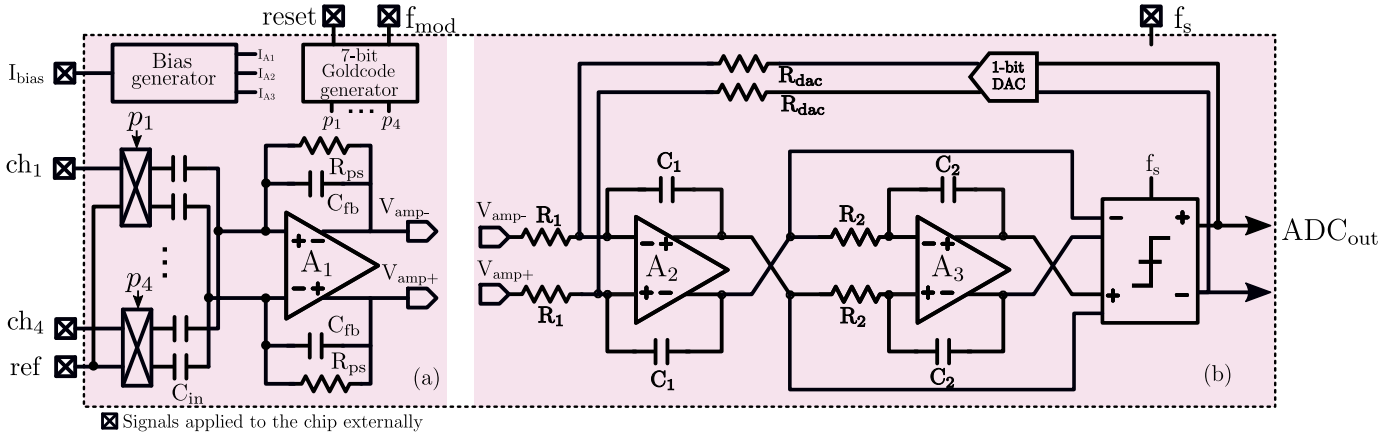

Fig. 10: Circuit block diagram of the proposed architecture:(a) PRBS-modulated amplifier, (b) $\Sigma\Delta$ modulator.

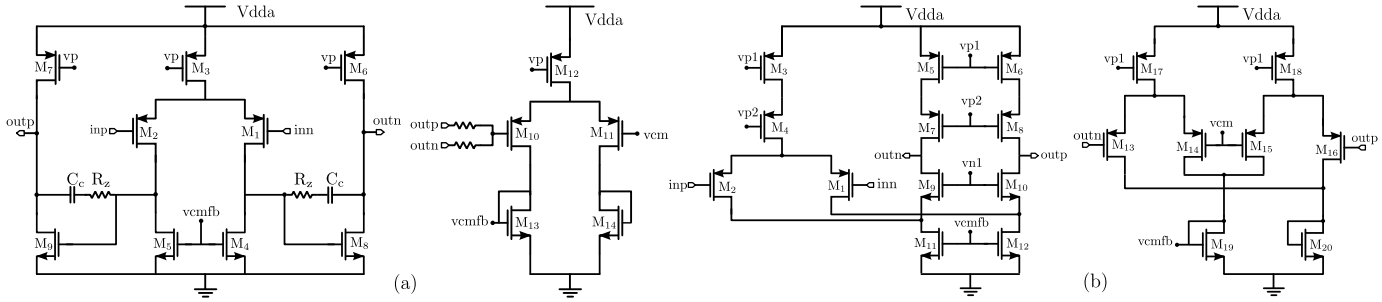

Fig. 11: Schematic implementation: (a) 2-stage opamp (A1, A2) & CMFB, (b) Folded-cascode opamp (A3) & CMFB.

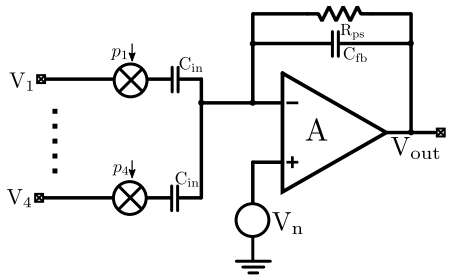

Fig. 12: Noise analysis of an N-input spread-spectrum amplifier

to V_{cm}= (0.9 V). The total power consumption of the spread-spectrum amplifier including biasing and CMFB is 23 μA from a 1.8V supply, corresponding to 5.75 μA per input.

To ensure a moderate accuracy, the value of C_{fb} is chosen equal to 100 fF with a unit capacitance of 50 fF. Higher values of C_{fb} would lead to higher C_{in} values for the given gain settings and thus lower impedances. For 4 inputs and a 7-bit Gold-code generator, a modulation frequency of 16 kHz or 32 kHz is sufficient. For f_{mod} = 35 kHz and L=127, the tones lie between 32 kHz and 251 Hz ($f_0 = \frac{32\,\text{kHz}}{127}$). The input capacitance C_{in}, combined with the mixer switch driven by modulation frequency f_{mod}, forms an impedance Z_{in} given by $1/(2f_{mod}C_{in})$. Assuming a maximum capacitance of $C_{in} = 3.2$ pF, the worst-case impedance ranges from 4.9 MΩ to 622 MΩ for f_{mod} and f_0, respectively.

From Fig. 12, the signal and noise gain of an N-input spread-spectrum amplifier can be written as:

$$V_{sig} = V_{in}(-\frac{C_{in}}{C_{fb}}); V_{n,out} = V_n(1 + \frac{N \cdot C_{in}}{C_{fb}}) \quad (7)$$

The input-referred noise is N times higher for an N-input amplifier as compared to a single-channel amplifier. On the other hand, N times more power can be spent on this single N-input amplifier, which results in an equal noise contribution per channel of both an N-input amplifier and N single-channel amplifiers. Note that, flicker noise is supressed if the signal is modulated before the amplifier.

B. $\Sigma\Delta$ ADC

For digitizing the modulated and summed signal inputs, a continuous-time $\Sigma\Delta$ modulator is implemented for its inherent anti-aliasing property. For the target application, there is a need to minimize the number of outgoing wires. Other ADCs such as SAR have the number of outputs equal to the number of bits. Additional circuitry such as an SPI is required to reduce the number of outgoing wires which might consume more area and power. For a total input bandwidth of 32 kHz and a resolution of 10 bits, a 2$^{\text{nd}}$ order orthornormal low-pass $\Sigma\Delta$ [32] (or weighted feed-forward topology) designed to operate at 7.8 MHz is selected for its optimal performance. The integrators are implemented using opamp-RC filters due to their high linearity. Alternative implementations such as g_mC integrators are more power-efficient as compared to opamp-RC integrators, however offer poorer linearity.

The performance of the modulator is determined by the first integrator stage. The errors originating in the second

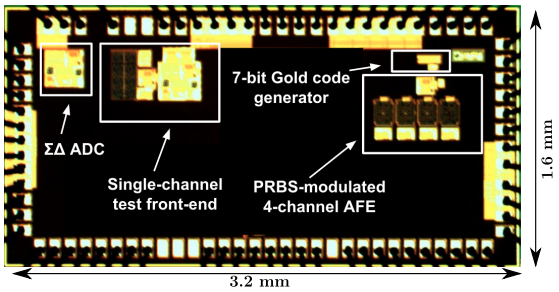

Fig. 13: Chip microphotograph

integrator and the following blocks are suppressed by the gain of the preceding blocks. For lower noise, a smaller input resistance ($<$300 kΩ) can be chosen. For a given integrator constant, for lower noise, a larger capacitance value is required leading to a higher opamp power consumption. To reduce loading of the previous stage and trading noise for lower power, R_1=R_2=512 kΩ and C_1=C_2=0.5 pF have been chosen. The common-mode voltage is at VCM=0.9 V. R_{dac} is chosen as 256 kΩ. The non-idealities of the integrator performance are simulated through behavioural simulations. To minimize the effect of finite DC gain and GBW on the performance of the modulator, a DC gain $>$ 85 dB and GBW $>$ 0.7 x f_s or 5 MHz would be sufficient. The impact of time-constant (RC) variations of the integrators is also modeled. For a variation upto $\pm$30%, there is a slight degradation in the performance. However, beyond $\pm$40%, the performance degrades significantly and may even become unstable. To achieve a high DC gain and high output swing, A_2 is implemented by a 2-stage opamp and A_3 by a folded-cascode opamp as shown in Fig. 11. A 1-bit comparator quantizes the signal, and a 1-bit DAC with four switches is implemented for its inherent linearity. To implement the 1-bit comparator and the summer, a multi-input two-stage dynamic comparator is implemented for its power efficiency. Its first stage provides amplification and is followed by a latching stage.

C. Generation of spread-spectrum codes

The PRBS codes are generated by a 7-stage Gold-code generator using two LFSRs, generating upto a maximum of 18 codes (See Table II). Four of these codes are required to modulate four inputs. Each LFSR has 7 delay flip-flops (DFF). At the start of the acquisition, all the outputs are cleared to 1 through a reset signal. The DFFs consume negligible area and power as compared to the rest of the circuitry. For an increasing number of input signals, the area occupied by WH code generator increases exponentially whereas for PRBS codes, the area of the corresponding generator increases by a few more gates.

V. Measurement Results

The prototype has been implemented in a standard 180 nm CMOS technology. Fig 14a shows the die photograph with a total chip area of about 5.12 mm^2 (3.2 mm x 1.6 mm) including the test structures and the IO ring. Fig 14a-b show

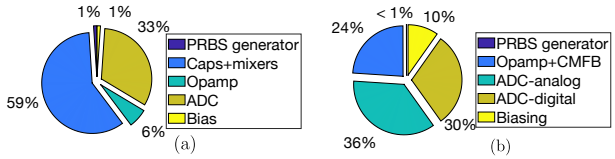

Fig. 14: (a) Area and (b) Power breakdown.

TABLE IV: Measured performance of 2nd order $\Sigma\Delta$ modulator

Parameter	Specification
Process	0.18 μm CMOS
Supply voltage	1.8 V
Current	36.3 μA
Bandwidth	16 kHz
Sampling frequency	7.8 MHz
SNDR	57.8 dB@16 kHz/50 dB @32 kHz
Dynamic range	68 dB
Walden FOM	0.87 pJ/conv
Area	0.09 mm^2

the area and power breakdown, respectively. A programmable-gain amplifier, a Gold-code based PRBS generator and a 2nd order $\Sigma\Delta$ modulator with a single outgoing wire are integrated for amplifying, digitizing and reading out of cardiac signals. The proposed PRBS-modulated multi-channel amplifier and $\Sigma\Delta$ ADC including biasing operate from 1.8V and draw 91.9 µA. The PRBS-modulated multichannel amplifier, PRBS generator and ADC occupy only 0.27 mm^2.

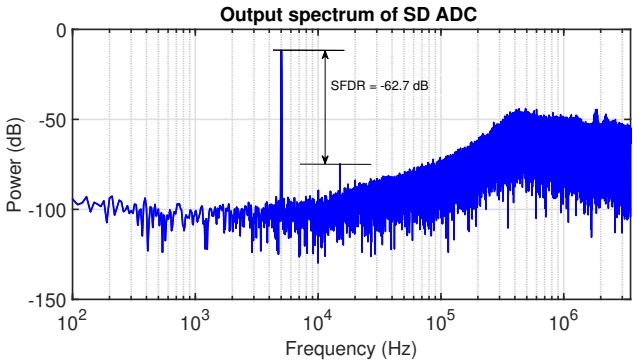

(a)

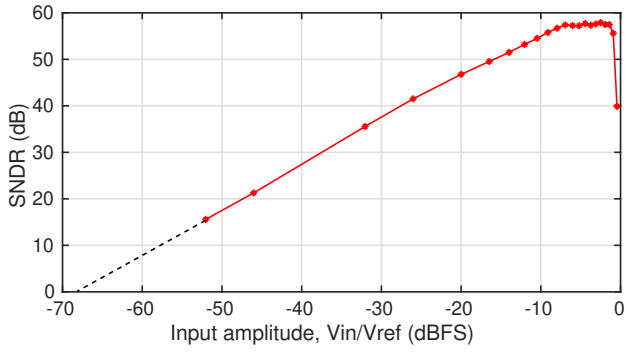

(b)

Fig. 15: Measured $\Sigma\Delta$ modulator performance (a) PSD plot for -2.4 dBFS input signal at 5 kHz (b) SNDR versus the input signal amplitude.

Fig. 15 shows the performance of the ADC. It achieves a peak SNDR of 57.8 dB measured at f_{in}= 5 kHz and

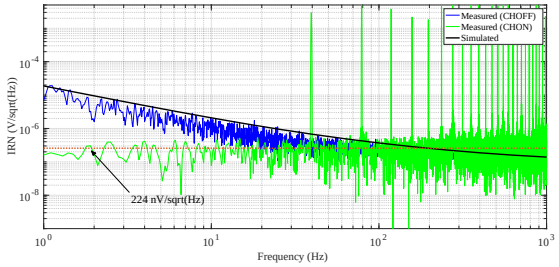

Fig. 16: Input-referred noise with PRBS modulation ON/OFF.

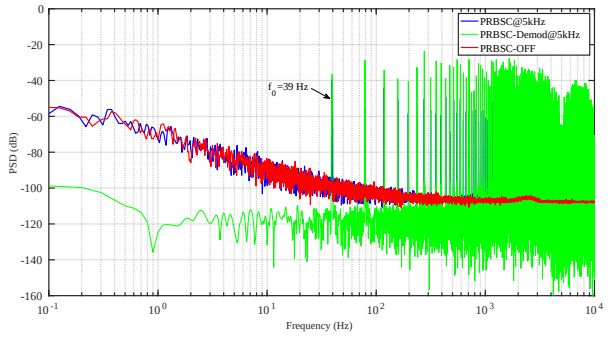

(a)

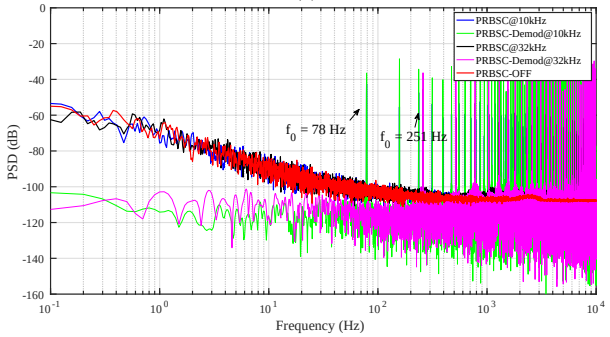

(b)

Fig. 17: Measured input-referred noise using PRBS modulation. (a) f_{mod} = 5 kHz, (b) f_{mod} = 10 kHz, f_{mod} = 32 kHz.

V_{in}@−2.4 dBFS), for a bandwidth of 16 kHz. For input signals lower than -52 dBFS the curve is extrapolated. As the input amplitude approaches its maximum limit, the curve tends to become flatter, but it remains stable [32]. The overall performance is summarized in Table IV. Fig. 16 shows the input-referred noise spectrum of the amplifier characterized by using a dynamic signal analyzer (SR785, Stanford Research Systems) capable of capturing low-frequency behaviour from 100 mHz. It shows the measured input referred noise before and after demodulation with f_{mod} = 5 kHz. The noise-floor is flat down to 1 Hz which shows that $\frac{1}{f}$ noise is removed by using PRBS modulation. The integrated noise for a bandwidth of 39 Hz is about 1.4 μVrms. The thermal noise density is at 224 nV/$\sqrt{}$(Hz). Fig. 17 characterizes the PRBS-modulated amplifier at f_{mod} = 5 kHz, 10 kHz and 32 kHz. For an f_{mod}@5 kHz, the lowest tone, f_0 is given by $\frac{5\,\text{kHz}}{127}$, i.e., 39 Hz which sets the maximum usable bandwidth, whereas, @10 kHz and 32 kHz, it occurs at 78 Hz and 251 Hz, respectively, as shown in Fig. 17b. It can be seen that the noise floor is higher for higher values of f_{mod}. Charge injection and clock feed-through associated with the MOSFET switches of the input chopper give rise to significant chopper noise. The magnitude of chopper noise increases proportionately with the modulation frequency as also observed and described in [33] and [34].

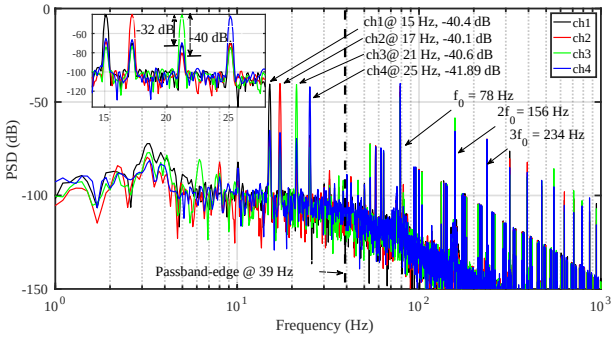

(a)

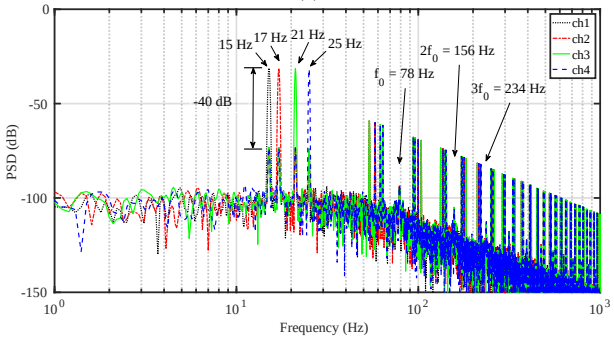

(b)

Fig. 18: (a) Measured spectrum of the demodulated and filtered signals upto a bandwidth $f_0/2$ at a modulation frequency of 10 kHz using a 2$^{\text{nd}}$ order digital low-pass filter; (b) Simulated spectrum on MATLAB.

In order to test the performance of the prototype, each of the channel inputs are simultaneously stimulated with a 5 mV_{pp} single-tone sinusoidal signal with a unique frequency i.e., 15 Hz, 17 Hz, 21 Hz and 25 Hz at a gain = 4 and modulated at 10 kHz. The Gold-codes are already known since the initial state of the DFFs are set to 1. For synchronization with the replica of the codes at the receiver end, one of the outputs of the generator is read out. A custom synchronization script is then used to reconstruct the other codes based on the known code sequence at 10 kHz. The combined output is read

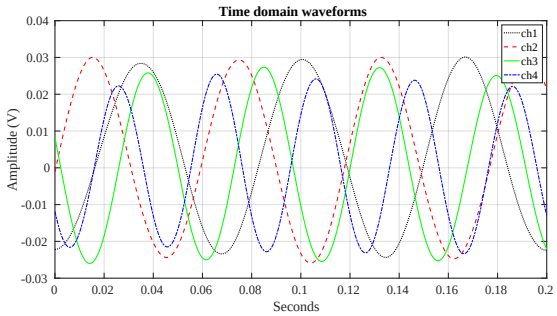

Fig. 19: Time-domain waveforms of the demodulated and filtered signals upto a bandwidth $f_0/2$ at a modulation frequency of 10 kHz using a 10$^{\text{th}}$ order digital low-pass filter.

out from the chip. Post-processing carried out on MATLAB involves demodulation using replicated codes and filtering with a 10^{th}-order digital low-pass filter (LPF) on the receiver side. Using a lower-order filter such as a 2^{nd}- or a 3^{rd}-order LPF results in lower performance as also shown in [6]. In Fig 18, the measured performance is compared with the results obtained from MATLAB simulations. With a 7-bit Gold-code generator ($L = 127$), the maximum achievable crosstalk performance is $-40\,\mathrm{dB}$ as shown in Fig. 18b. In Fig. 18a, the measured crosstalk performance varies between $-32\,\mathrm{dB}$ and $-40\,\mathrm{dB}$ depending on the Gold codes. The degradation in crosstalk performance in the practical setup can be attributed to non-zero cross-correlation between the codes and the use of a shared reference [35]. PRBS modulation upmodulates flicker noise and offset to the tones at f_0, $2\times f_0$ ... f_{mod}. For large circuit offset, the tones are larger. In Fig. 18b, the tones present bewteen $40\,\mathrm{Hz}$ and $78\,\mathrm{Hz}$ are intermodulation tones. The intermodulation tones result due to the interaction between the signal inputs and the modulation frequency. The inputs at $15\,\mathrm{Hz}$, $17\,\mathrm{Hz}$, $21\,\mathrm{Hz}$ and $25\,\mathrm{Hz}$ result in intermodulation tones at $63\,\mathrm{Hz}$, $61\,\mathrm{Hz}$, $57\,\mathrm{Hz}$ and $53\,\mathrm{Hz}$, respectively due to f_0 tone at $78\,\mathrm{Hz}$. The low-pass filter attenuates the input frequencies that are closer to its cut-off frequency (ch3 and ch4) due to its 10^{th} - order roll-off. The slight variation in amplitude between ch1 ($-40.4\,\mathrm{dB}$) and ch2 ($-40.1\,\mathrm{dB}$) could be attributed to a mismatch in gain between the channels. Fig. 19 shows the recovered inputs in the time domain.

Table V presents a summary of the proposed system performance and a benchmark with state-of-the-art modulation approaches for multi-channel recording systems. The proposed system is designed for acquiring unipolar atrial electrograms with a shared reference. Comparing with systems that use orthogonal codes such as [7] which requires look-up tables (or on-chip memory), the proposed system includes an integrated PRBS generator which consumes negligible power and area. Also, the number of bondpads/input in the proposed approach is $1\times$, whereas other implementations such as [7], [9] or [6] use $2\times$ the number of inputs. In comparison to [4] and [9], the proposed system consumes less area/channel. The proposed method is attractive for applications with strict area constraints for low-resolution signal acquisition, such as wavefront mapping.

TABLE V: Comparison with modulation approaches for multi-channel systems

	JSSC'20 [7]	TCAS'21 [6]	TBCAS'19 [4]	TVLSI'19 [9]	This work
Modulation/Mutliplexing	WH/CDM	WH/CDM	FM/FDM	OFC/CDM	PRBS/CDM
Type of biosignal	EMG	EEG	EEG	ECG	AEG
Type of recording	Bipolar	Bipolar	Unipolar	Bipolar	Unipolar
Reference electrode	Dedicated	Dedicated	Shared	Dedicated	Shared
Look-up table required	Yes	Yes	No	No	No
Bondpads/input	2	2	1	2	1
No. of channels	15	4	4	2	4
Shared blocks	LNA,ADC	ADC	ADC	LNA	LNA,ADC
ADC architecture	Async.	SAR	SAR	-	ΣΔ
Serializer	Yes	Yes	Yes	No	Yes
Ratio wirecount	15:1	4:1	4:1	1:1	4:1
Current/channel (uA)	9.2	1.5	190	0.36	20.7
Noise density $\frac{nV}{\sqrt{Hz}}$	155	95.9	63	130	240
LNA Gain (dB)	40-56	45.3	-	40	12-30.1
Area/ch (mm^2)	0.019	0.08	1	0.34	0.067
Process (μm)	0.18	0.18	0.35	0.13	0.18

VI. Conclusions and Future Work

This paper proposes a novel design strategy to develop optimal spread-spectrum analog front-ends. A structured classification of modulation strategies orthogonalized by their degrees of freedom is proposed to identify possible techniques for acquiring analog signals. The proposed design method is validated by implementing a 4-input PRBS modulated spread-spectrum recording system in $0.18\mu m$ CMOS process, which consists of a shared amplifier, a shared ΣΔ ADC, and an on-chip Gold code generator occupying $0.067\,\mathrm{mm}^2$ and consuming $23\,\mu\mathrm{A}$ per channel input.

Acknowledgment

The authors would like to acknowledge the support and funding from NWO and the Dutch Heart Foundation (Project number: 14728). The authors wish to thank Prof. Earl McCune for his contributions in the early stage of this work. The authors would like to thank Prof. Natasja de Groot from Erasmus Medical Centre, Rotterdam for providing the invasively acquired AEGs.

References

[1] A. Yaksh, L. J. van der Does, C. Kik, P. Knops, F. B. Oei, P. C. van de Woestijne, J. A. Bekkers, A. J. Bogers, M. A. Allessie, and N. M. de Groot, "A novel intra-operative, high-resolution atrial mapping approach," *Journal of Interventional Cardiac Electrophysiology*, vol. 44, no. 3, pp. 221–225, 2015.

[2] C. Mora Lopez, J. Putzeys, B. C. Raducanu, M. Ballini, S. Wang, A. Andrei, V. Rochus, R. Vandebriel, S. Severi, C. Van Hoof, S. Musa, N. Van Helleputte, R. F. Yazicioglu, and S. Mitra, "A neural probe with up to 966 electrodes and up to 384 configurable channels in 0.13 μm soi cmos," *IEEE Transactions on Biomedical Circuits and Systems*, vol. 11, no. 3, pp. 510–522, 2017.

[3] M. Sharma, H. J. Strathman, and R. M. Walker, "Verification of a rapidly multiplexed circuit for scalable action potential recording," *IEEE Transactions on Biomedical Circuits and Systems*, vol. 13, no. 6, pp. 1655–1663, 2019.

[4] J. Warchall, P. Theilmann, Y. Ouyang, H. Garudadri, and P. P. Mercier, "Robust biopotential acquisition via a distributed multi-channel fm-adc," *IEEE Transactions on Biomedical Circuits and Systems*, vol. 13, no. 6, pp. 1229–1242, Dec 2019.

[5] ——, "22.2 a rugged wearable modular exg platform employing a distributed scalable multi-channel fm-adc achieving 101db input dynamic range and motion-artifact resilience," in *2019 IEEE International Solid-State Circuits Conference - (ISSCC)*, Feb 2019, pp. 362–364.

[6] R. Ranjandish and A. Schmid, "Walsh-hadamard-based orthogonal sampling technique for parallel neural recording systems," *IEEE Transactions on Circuits and Systems I: Regular Papers*, vol. 68, no. 4, pp. 1740–1749, 2021.

[7] J. H. Park, T. Tang, L. Zhang, K. A. Ng, G. G. L. Gammad, S. C. Yen, and J. Yoo, "A 15-channel orthogonal code chopping instrumentation amplifier for area-efficient, low-mismatch bio-signal acquisition," *IEEE Journal of Solid-State Circuits*, vol. 55, no. 10, pp. 2771–2780, 2020.

[8] C. C. Enz and G. C. Temes, "Circuit techniques for reducing the effects of op-amp imperfections: autozeroing, correlated double sampling, and chopper stabilization," *Proceedings of the IEEE*, vol. 84, no. 11, pp. 1584–1614, Nov 1996.

[9] P. Khatavkar and S. Aniruddhan, "432 nw per channel 130 nv/rthz ecg acquisition front end with multifrequency chopping," *IEEE Transactions on Very Large Scale Integration (VLSI) Systems*, vol. 27, no. 9, pp. 2021–2032, Sep. 2019.

[10] Y. Tsai, F. Lee, T. Chen, and T. Lin, "A 2-channel -83.2dB crosstalk $0.061\mathrm{mm}^2$ CCIA with an orthogonal frequency chopping technique," in *2015 IEEE International Solid-State Circuits Conference - (ISSCC) Digest of Technical Papers*, Feb 2015, pp. 1–3.

[11] Yen-Po Chen, D. Blaauw, and D. Sylvester, "A 266nW multi-chopper amplifier with 1.38 noise efficiency factor for neural signal recording," in *2014 Symposium on VLSI Circuits Digest of Technical Papers*, June 2014, pp. 1–2.

[12] A. Tang, "Bandpass spread spectrum clocking for reduced clock spurs in autozeroed amplifiers," in *ISCAS 2001. The 2001 IEEE International Symposium on Circuits and Systems (Cat. No.01CH37196)*, vol. 1, 2001, pp. 663–666 vol. 1.

[13] J. E. C. Brown, "Chopper-stabilized amplifier with spread-spectrum clocking," U.S. Patent US5115202A, Apr. 1991.

[14] Z. Ignjatovic, "Blue-noise-modulated sigma-delta analog-to-digital converter," U.S. Patent US7649481B2, Jan. 2010.

[15] S. Rout, M. Mangia, F. Pareschi, G. Setti, R. Rovatti, and W. A. Serdijn, "Rakeness-based compressed sensing of atrial electrograms for the diagnosis of atrial fibrillation," in *2019 IEEE International Symposium on Circuits and Systems (ISCAS)*, May 2019, pp. 1–5.

[16] M. Maslik, T. S. Lande, and T. G. Constandinou, "A clockless method of flicker noise suppression in continuous-time acquisition of biosignals," in *2018 IEEE Biomedical Circuits and Systems Conference (BioCAS)*, Oct 2018, pp. 1–4.

[17] S. Sankaran and K. K. O, "A ultra-wideband amplitude modulation (am) detector using schottky barrier diodes fabricated in foundry cmos technology," *IEEE Journal of Solid-State Circuits*, vol. 42, no. 5, pp. 1058–1064, 2007.

[18] K. Igarashi and K. Kikuchi, "Optical signal processing by phase modulation and subsequent spectral filtering aiming at applications to ultrafast optical communication systems," *IEEE Journal of Selected Topics in Quantum Electronics*, vol. 14, no. 3, pp. 551–565, 2008.

[19] M. Alioto, "Trends in hardware security: From basics to asics," *IEEE Solid-State Circuits Magazine*, vol. 11, no. 3, pp. 56–74, 2019.

[20] G. Mazzini, G. Setti, and R. Rovatti, "Chaotic complex spreading sequences for asynchronous ds-cdma. i. system modeling and results," *IEEE Transactions on Circuits and Systems I: Fundamental Theory and Applications*, vol. 44, no. 10, pp. 937–947, 1997.

[21] S. Hengstler, D. Kasilingam, and A. Costa, "A novel chirp modulation spread spectrum technique for multiple access," in *IEEE Seventh International Symposium on Spread Spectrum Techniques and Applications,*, vol. 1, 2002, pp. 73–77 vol.1.

[22] A. M. R. Dixon, E. G. Allstot, D. Gangopadhyay, and D. J. Allstot, "Compressed sensing system considerations for ecg and emg wireless biosensors," *IEEE Transactions on Biomedical Circuits and Systems*, vol. 6, no. 2, pp. 156–166, April 2012.

[23] R. Starreveld, L. J. van der Does, and N. D. de Groot, "Anatomical hotspots of fractionated electrograms in the left and right atrium: do they exist?" *EP Europace*, vol. 21, pp. 60–72, 2019.

[24] A. B. Carlson, P. B. Crilly, and J. Rutledge, *Communication Systems: An Introduction to Signals and Noise in Electrical Communication*. McGraw-Hill, 2002.

[25] W. A. Gardner, A. Napolitano, and L. Paura, "Cyclostationarity: Half a century of research," *Signal Processing*, vol. 86, no. 4, pp. 639 – 697, 2006. [Online]. Available: http://www.sciencedirect.com/science/article/pii/S0165168405002409

[26] D. V. Sarwate and M. B. Pursley, "Crosscorrelation properties of pseudorandom and related sequences," *Proceedings of the IEEE*, vol. 68, no. 5, pp. 593–619, 1980.

[27] H. Roefs, "Binary sequences for spread-spectrum multiple-access communication (ph.d. thesis abstr.)," *IEEE Transactions on Information Theory*, vol. 24, no. 2, pp. 277–277, 1978.

[28] J. Proakis and M. Salehi, *Digital Communications*. McGraw-Hill, 2008. [Online]. Available: https://books.google.nl/books?id=ABSmAQAACAAJ

[29] L. Welch, "Lower bounds on the maximum cross correlation of signals (corresp.)," *IEEE Transactions on Information Theory*, vol. 20, no. 3, pp. 397–399, 1974.

[30] R. Mutagi, "Pseudo noise sequences for engineers," *Electronics & communication engineering journal*, vol. 8, no. 2, pp. 79–87, 1996.

[31] R. Pickholtz, D. Schilling, and L. Milstein, "Theory of spread-spectrum communications - a tutorial," *IEEE Transactions on Communications*, vol. 30, no. 5, pp. 855–884, May 1982.

[32] S. Rout and W. Serdijn, "High-pass $\Sigma\Delta$ converter design using a state-space approach and its application to cardiac signal acquisition," *IEEE Transactions on Biomedical Circuits and Systems*, vol. 12, no. 3, pp. 483–494, 2018.

[33] J. Xu, Q. Fan, J. H. Huijsing, C. Van Hoof, R. F. Yazicioglu, and K. A. A. Makinwa, "Measurement and analysis of current noise in chopper amplifiers," *IEEE Journal of Solid-State Circuits*, vol. 48, no. 7, pp. 1575–1584, 2013.

[34] D. Drung and J.-H. Storm, "Ultralow-noise chopper amplifier with low input charge injection," *IEEE Transactions on Instrumentation and Measurement*, vol. 60, no. 7, pp. 2347–2352, 2011.

[35] O. Malekzadeh-Arasteh, A. R. Danesh, A. H. Do, Z. Nenadic, and P. Heydari, "An analysis of cmrr degradation in multi-channel biosignal recording systems," *IEEE Transactions on Circuits and Systems II: Express Briefs*, vol. 68, no. 1, pp. 151–155, 2021.

Jane Doe Biography text here.

You can push biographies down or up by placing a

before or after them. The appropriate use of

depends on what kind of text is on the last page and whether or not the columns are being equalized.